inorganics

MDPI

Article

Sheaf-like Manganese-Doped Zinc Silicate with Enhanced Photoluminescence Performance

Xiaohong Li [1], Xiaozhen Zhang [1,*], Yongzhi Yu [1], Leying Wang [1], Si Cheng [1], Hongquan Zhan [1,*], Runyuan Liu [2] and Renhua Chen [2]

[1] School of Materials Science and Engineering, Jingdezhen Ceramic University, Jingdezhen 333403, China; lihong7178@163.com (X.L.); yuyongzhi1120@126.com (Y.Y.); wly8858@163.com (L.W.); sicheng0326@163.com (S.C.)

[2] Jiangxi Jinhuan Pigments Co., Ltd., Yichun 336000, China; 18879578701@163.com (R.L.); chenrenhua1979@126.com (R.C.)

* Correspondence: zhangxiaozhen@jcu.edu.cn (X.Z.); zhq_0425@163.com (H.Z.)

Abstract: Sheaf-like manganese-doped zinc silicate (Mn-doped Zn_2SiO_4) was successfully synthesized without surfactant by hydrothermal route using manganese acetate, zinc nitrate, and sodium silicate as precursors. The structure, morphology, and optical properties were well investigated by various analytical techniques, such as X-ray diffraction (XRD), a scanning electron microscope (SEM), a transmission electron microscope (TEM), and photoluminescence (PL). The results showed the enhancement of crystallinity and an increase in the length of the as-prepared sample, which was achieved by prolonging the hydrothermal time. Based on the analysis of the XRD pattern, it can be stated that the sheaf-like Mn-doped Zn_2SiO_4 possesses a large lattice distortion compared to pure Zn_2SiO_4. Moreover, it was observed that hydrothermal times played a crucial role in the PL property. The PL peak intensity of samples located at 522 nm generally increased with the increase in reaction time in the range of 12–48 h. However, when the treating time reached 72 h, the property of PL decreased. The results of the PL spectra showed that Mn-doped Zn_2SiO_4 obtained by a hydrothermal time of 48 h displayed an efficient luminescent performance. The key to the high PL property mainly lies in the sheaf-like structure and large lattice distortion.

Keywords: sheaf-like structure; Mn doping; zinc silicate; photoluminescence

Citation: Li, X.; Zhang, X.; Yu, Y.; Wang, L.; Cheng, S.; Zhan, H.; Liu, R.; Chen, R. Sheaf-like Manganese-Doped Zinc Silicate with Enhanced Photoluminescence Performance. *Inorganics* **2023**, *11*, 407. https://doi.org/10.3390/inorganics11100407

Academic Editors: Richard Dronskowski, Christian Julien, Rainer Niewa, Guido Kickelbick, Alexander S. Novikov, Gary Hix and Hans-Conrad zur Loye

Received: 5 September 2023
Revised: 9 October 2023
Accepted: 10 October 2023
Published: 16 October 2023

1. Introduction

The search for inorganic luminescent materials with earth-rich and low-cost elements is important to promote their applications in optics and optoelectronics, biological, and medical diagnostics [1–4]. According to their composition and chemical structure, the luminescent materials include silicate [5], aluminate [6–8], sulfide [9], phosphate [10], tungstate [11], molybdate [12], vanadate [13] and halide [14]. All of them have good, stable physical and chemical properties and are considered to be very promising phosphors. Luminescent materials of sulfide have gradually been phased out because of low brightness, short afterglow, and poor chemical stability in the air. Compared to the series of sulfides, aluminate materials have the advantages of high brightness, long afterglow, as well as good color rendering. However, some obvious defects, such as poor moisture resistance and single luminescent color, have significantly limited their applications. Phosphate luminescent materials include strontium pyrophosphate, lanthanum phosphate, phosphate halide, and a zinc phosphate system. Phosphate has excellent characteristics such as safety, pollution-free, high stability, and especially good luminous properties in ultraviolet and vacuum ultraviolet excitation. However, its luminous color is monotonous, it has poor water resistance, and it decomposes in water, resulting in a reduced luminous performance. In some cases, it completely loses its luminous performance, which limits its development to a certain extent [15]. Compared with other matrix materials, molybdate luminescent

materials have the advantages of high color purity, long fluorescence life, and low synthesis temperature and have shown broad application prospects in lighting, temperature sensing, biological imaging, and other fields. However, the temperature characteristics, crystal field environment, and quantum efficiency stability of phosphors need to be further explored [16]. The special structure of tungstate makes it highly doped with rare earth ions. In order to find new solid luminescent materials, the luminescent materials based on tungstate are becoming the research hotspot of solid lighting in the world. However, the research on tungstate luminescent materials is still in its infancy, the system is not rich enough, the luminescence mechanism is not clear enough, and the preparation method cannot adapt to large-scale production, and these obstacles affecting the practical application of tungstate luminescent materials need to be further explored [17]. Phosphors based on vanadate have attracted much attention due to their low synthesis temperature, stable chemical properties, and good thermal stability. It is good for a variety of flat panel display information displays, human medical health, lighting sources, particle detection and recording, optoelectronic devices, and agricultural, military, and other fields of support materials [18]. Organic–inorganic metal halides (OIMHs) have become the focus of current luminescence research due to their excellent luminescence properties. The advantages of OIMHs are mainly reflected in their high luminous quantum efficiency (PLQY) and wide spectrum emission. OIMH is a strong candidate for the realization of single-component white light emitting LEDs, which can cover the entire visible light region with a single-component emission spectrum through component regulation. At present, the strategies to improve the PLQY of OIMH compounds are mainly through reducing the crystal structure dimension, doping the luminescence center ion, changing the distance between the coordination polyhedral, and adjusting the structure through halogen substitution [19–21]. Among various materials, silicate-based composites have attracted increasing research interests as potentially commercial luminescent materials owing to strong environmental adaptability, reliable chemical inertness, excellent moisture resistance, high brightness, low cost, and facile synthesis [22,23].

Zinc silicate (Zn_2SiO_4) is a very important luminescent material. Barthou, C. et al. found that the optical properties of manganese-activated zinc silicate $Zn_{2(1-x)}Mn_{2x}SiO_4$ are investigated using pulse selective photon excitation. The light response due to the $^4T_{1g}$-$^6A_{1g}$ transition is directly linked to the relative concentration of isolated Mn^{2+} and Mn^{2+} pairs in this structure. The decay curves can be fitted by a diffusion-limited relaxation mechanism by considering two types of centers with radiative lifetimes of T0 equal to 15 and 1.75 ms, respectively [24]. Zn_2SiO_4 has been applied in broad areas, covering phosphor hosts, paints, as well as electronic insulators due to its excellent physical and chemical properties [25–27]. In the field of luminescence, the doping of Zn_2SiO_4 via introducing additional elements into the Zn_2SiO_4 framework plays a central role in modulating the electronic, luminescent, and other physical performances. Mn-doped Zn_2SiO_4 as a green phosphor has attracted much attention, owing primarily to its high luminescent efficiency and chemical stability. A small amount of Mn^{2+} replaces Zn^{2+} to form a luminescent center, and a green phosphor with high luminosity and good color purity can be obtained. However, its afterglow time is long, and its afterglow time (t) is about 11.9 ms, which can easily produce a picture lag effect in the display, limiting its application and development in PDP. Recently, W-LED has been called the fourth-generation lighting source because of its environmental protection, energy-saving capabilities, and high luminous efficiency. As far as the current trend is concerned, the main technical way to produce white light is still through phosphor conversion white LEDs. There are two main methods: the first is to use a blue light chip to excite yellow phosphor; due to the lack of red light in the emission spectrum and the lack of green light, the white light will cause the relative color temperature to be high and the color rendering index to be low. Another method is to use ultraviolet or near-ultraviolet chips to excite three primary color phosphors (red phosphors, green phosphors, and blue phosphors), and the white light obtained by this method has a higher color rendering index and good stability. However, at present, phosphors that can match

near-ultraviolet light or ultraviolet light well and have high thermal stability and luminous efficiency are still lacking. Therefore, it is of great theoretical and practical significance to study and improve the properties of Zn_2SiO_4: Mn green luminescent materials from the perspective of synthesis technology and doping modification [28–30]. Further, the intensity of green emissions could be tuned by adding an Mn ion, which is beneficial to broadening its application range in display and lighting, white-light-emitting diodes (W-LED), fingerprint identification, information storage, and anti-counterfeit technology, and using both photoluminescence and magnetic properties, there is the potential application for W-LEDs in the fields of magneto-optical and spintronic device areas [27,31–34].

Over the past few years, strenuous efforts have been devoted to synthesizing Mn-doped Zn_2SiO_4 through different synthesis routes, such as the solid-state reaction method [35], sol–gel method [36], polymer precursor method [37], spray pyrolysis method [38], and hydrothermal method [39]. Among these methods, hydrothermal processing has great advantages, covering better metal ion distribution, lower costs, and controllable morphology. It is well known that the structures, sizes, and morphologies of functional materials can significantly influence their properties. Therefore, controlled morphologies, sizes, and structures of the Zn_2SiO_4 matrix are an effective technique for advancing Zn_2SiO_4 phosphors with high luminescence efficiency. A variety of Zn_2SiO_4 nano- or microstructures have been reported [40–44]. For example, Jung Sang Cho et al. reported a spray-drying method for preparing densely structured Zn_2SiO_4:Mn phosphor particles, which are easy to control through different additives (citric acid, sucrose, and dextrin) [40]. It was found that the dextrin-assisted precursor particles were turned into dense spherically shaped particles, with a mean particle size of 1.3 μm and the high crystallinity of a pure Zn_2SiO_4 phase, which showed the highest luminescence intensity. Wan et al. designed a one-dimensional rice-like Mn-doped Zn_2SiO_4 through a two-stage aging–crystallization hydrothermal route without further calcining treatment [43]. It was found that the appropriate aging temperature and aging time played important roles in obtaining pure hexagonal structural Zn_2SiO_4, which showed good hydrothermal stability and base-resistant properties but bad acid-resistant properties. Nevertheless, there are few reports in the literature on the influences of morphology on luminescent properties.

Here, we demonstrated that a sheaf-like Mn-doped Zn_2SiO_4 composed of accumulated nanorods was prepared by the hydrothermal method. The raw materials of manganese acetate ($Mn(OOCHC)_2$), zinc nitrate ($Zn(NO_3)_2{\cdot}6H_2O$), and sodium silicate ($Na_2SiO_3{\cdot}9H_2O$) were used as the precursors in the hydrothermal reaction. The effects of the hydrothermal time on the microstructure and photoluminescence (PL) properties are systematically investigated. The diameter and length of the rod were gradually increased by just prolonging the hydrothermal time. Through the present way, the enhancement of the large lattice distortion and sheaf-like microstructure can be achieved simultaneously, which are two favorable factors for promoting the PL performance of Mn-doped Zn_2SiO_4. The effects of the morphology on the luminescent performance are discussed.

2. Experimental Section

2.1. Sample Synthesis

The optimization of Mn centration was 8 mol %, according to the reported literature [36]. In a standard synthesis, 0.64 mmol manganese acetate ($Mn(OOCHC)_2$) was dissolved in 8 mmol zinc nitrate ($Zn(NO_3)_2{\cdot}6H_2O$) solutions. The Mn^{2+}/Zn^{2+} ratios in the solutions were 0.08. Then, 4 mmol sodium silicate ($Na_2SiO_3{\cdot}9H_2O$) solutions were gradually dropped into the above solution. In sequence, the mixture was placed into a separate Teflon container within the hydrothermal vessel and transferred to an oven. After aging at 100 °C for 12 h, the oven was heated at 200 °C for varying times of 12, 24, 48, and 72 h, respectively, with a ramp rate of 5 °C/min. The white powder was collected by filtrating and washing with deionized water several times, followed by drying at 80 °C for 4 h under vacuum, and then annealed at 600 °C for 2 h at a heating rate of 5 °C/min.

Finally, the white products were obtained and denoted as Mn-Zn_2SiO_4-x, where x stands for the relative hydrothermal reaction time.

2.2. Characterization

The phase structure and phase purity of as-prepared samples were evaluated by X-ray diffraction (XRD, D8 Advance, Bruker, Mannheim, Germany) using Cu Kα radiation (λ = 1.5418 Å) at tube voltage of 40 kV and tube current of 40 mA. Intensities were collected in the 2-theta range between 10 and 80° with a step size of 0.02° and a measuring time of 0.2 s at each step. For the calculations of the cell parameters and bond length, Rietveld refinement was carried out by the Total Pattern Solution (TOPAS) program. For refinement, the intensities of XRD were obtained in the 2-theta range between 10 and 120° with a step size of 0.02° and a measuring time of 6 s at each step. A scanning electron microscope (SEM, SU-8010, HITACHI, Tokyo, Japan) and transmission electron microscope (TEM, JEM-2010, JEOL, Tokyo, Japan) were used to investigate the morphological and structural features of the samples. X-ray photoemission spectroscopy (XPS) was measured using a Thermo ESCAlab 250Xi (Thermo Electron Corporation, Waltham, MA, USA) to explore the elements and chemical structure. The sample was irradiated with monochromated Al Kα X-rays (1486.6 eV), the pass energy was 20 eV, and the energy step size was 0.1 eV. The depth profile was achieved by Ar bombardment in the chamber. The photoluminescence (PL) spectra were measured with a fluorescence spectrophotometer (F-7000, Hitachi, Tokyo, Japan) with an excitation wavelength of 250 nm from xenon lamp.

3. Results and Discussion

3.1. Crystal Phase and Lattice Distortion

Figure 1 shows the XRD patterns of as-obtained Mn-doped Zn_2SiO_4 treated for different times in the range of 12–72 h under a post-heating temperature of 600 °C. All of the Mn-doped Zn_2SiO_4 phosphors show similar diffraction patterns; the synthesized phase above 24 h is a pure phase (Zn_2SiO_4), there is no second phase, and the crystallization degree is better, indexed as almost pure rhombohedral Zn_2SiO_4 (JCPDS card No. 37-1485), indicating that all samples have, basically, the same crystal structure. It is also observed that introducing Mn into Zn_2SiO_4 does not bring obvious crystal changes, owing to matching ionic radii and coordination numbers (0.80 Å for Zn^{2+} and 0.74 Å for Mn^{2+} (CN = 4)) [45], but the diffraction peak intensity for Mn-doped Zn_2SiO_4 gradually increases with the hydrothermal time. This suggests that the crystal growth of Mn-doped Zn_2SiO_4 is promoted by the increase in reaction time.

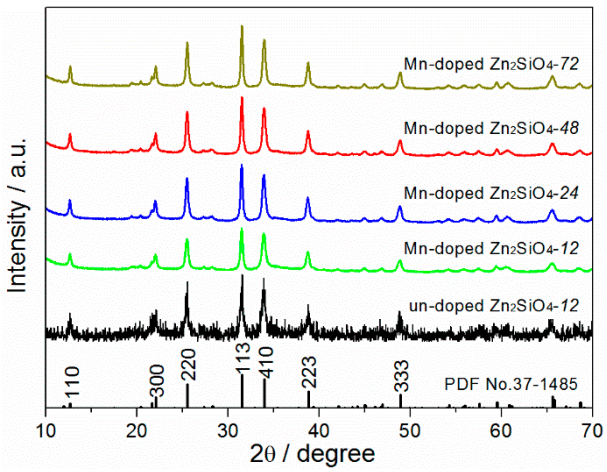

Figure 1. XRD patterns of the Mn-doped Zn_2SiO_4 phosphor synthesized at different hydrothermal time with a heating treatment of 600 °C.

Although the ionic radii of Mn^{2+} is close to that of Zn^{2+}, the introduction of Mn^{2+} inevitably leads to the lattice distortion of as-prepared samples to some extent and has a great influence on the PL property. The lattice distortion of sheaf-like Mn-doped Zn_2SiO_4 can be calculated in the following Gaussian–Cauchy equation [46]:

$$\frac{K\lambda}{(\delta 2\theta)Lcon\theta_0} = 1 - \frac{16e^2}{(\delta 2\theta)^2 cot^2\theta_0}$$

where ($\delta 2\theta$) is the width of the integral, K is the constant of Scherrer (K is equal to 1 when the width of the integral is used in this function), λ is the wavelength of X-ray (λ is equal to 0.15418 nm using X-ray diffraction with Cu Kα radiation), θ_0 is the position of the peak in the XRD pattern, L is the average size of the grain, and e is the maximum lattice distortion of the sheaf-like Mn-doped Zn_2SiO_4. The detailed results of the calculated lattice distortion of different samples are shown in Table 1. It is revealed that the lattice distortion of the samples reached the maximum when the treatment time was 48 h.

In order to further explore the influence of Mn^{2+} substitution on the structure of Zn_2SiO_4, the cell parameters in the Mn-Zn_2SiO_4-x lattice are calculated by Rietveld structural refinement with the TOPAS program. The refined results show that all samples fit well with Zn_2SiO_4 (JCPDS PDF#37-1485), and the R-weighted pattern (Rwp) was within the acceptable error range, suggesting that the refinement results are reliable. Figure 2 shows the Rietveld refinement results for the X-ray diffraction pattern for the Mn-Zn_2SiO_4-x (x = 12, 24, 48, and 72 h). The cell parameters of each composition are listed in Table 1. Compared with pure Zn_2SiO_4, the cell parameter of Mn-doped Zn_2SiO_4 slightly decreases as a result of the small ionic radii of Mn^{2+}. In addition, it can be seen that the cell parameters decrease when increasing the hydrothermal time from 12 to 72 h, which is attributed to the increasing crystallinity.

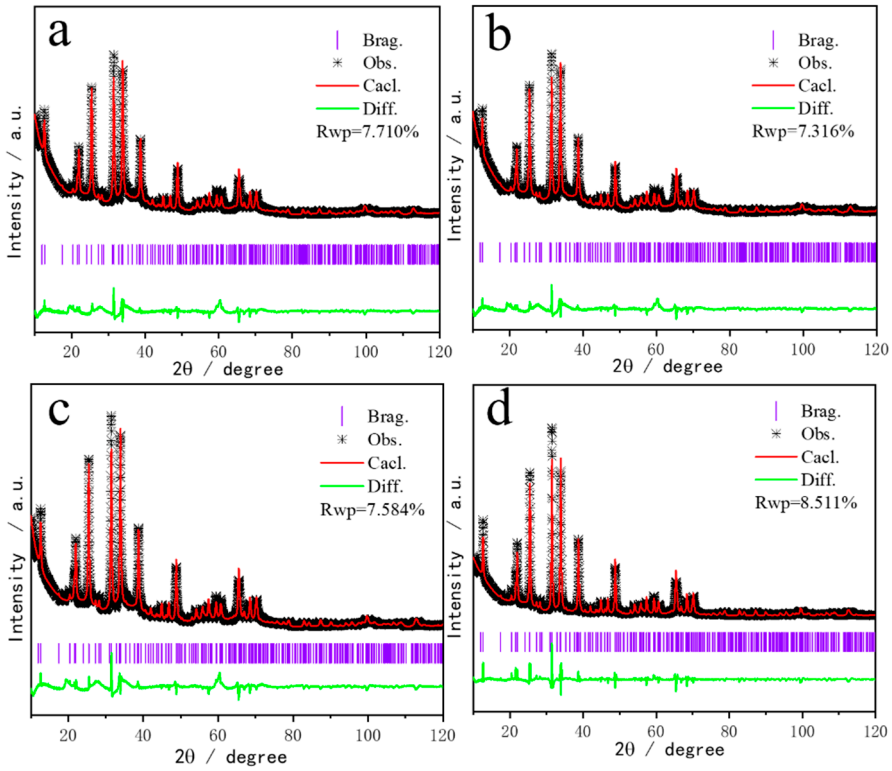

Figure 2. The Observed and calculated X-ray diffraction patterns obtained by Rietveld refinement for Mn-Zn_2SiO_4-12 (**a**), Mn-Zn_2SiO_4-24 (**b**), Mn-Zn_2SiO_4-48 (**c**), and Mn-Zn_2SiO_4-72 (**d**).

Table 1. The lattice parameters, average size of grain (L) and the maximum lattice distortion (e) of Mn-Zn_2SiO_4-x samples.

Samples	Peak Position	L/nm	E×1000	a, b (Å)	c (Å)	Cell Volume (Å^3)
JCPDS No. 37-1485	/	/	/	13.9381	9.310	1566.3
x = 12	(110) and (220)	31.04	4.16	13.9273	9.309	1563.8
x = 24	(110)and (220)	34.96	4.43	13.9242	9.306	1562.6
x = 48	(110)and (220)	38.87	4.98	13.9188	9.305	1561.2
x = 72	(110) and (220)	41.58	4.02	13.9136	9.297	1558.7

3.2. X-ray Photoemission Spectroscopy (XPS) Analysis

The XPS measurement was also performed to investigate the chemical composition and state of Mn, Zn, Si, and O in Mn-Zn_2SiO_4-48. Taking into account the specimen charging, the binding energies were corrected by referring to C (1s) at the 284.8 eV peak position. As shown in Figure 3a, the survey spectrum of XPS shows that the Zn, Si, and O elements are the main components of Mn-Zn_2SiO_4-48, and the peak of the Mn element is weak due to its low doping concentration. The Zn 2p spectrum (Figure 3b) shows two peaks at 1044.9 and 1021.9 eV, corresponding to the binding energies of Zn 2p1/2 and Zn 2p3/2, respectively. For the Si 2p spectrum (Figure 3c), the peak with binding energy at 102.5 eV is attributed to the (SiO_4) bond. Figure 3d shows that the binding energy is located at 102.5 eV, corresponding to the Si-O bond. The high-resolution Mn 2p spectrum in Figure 3e was deconvoluted into three peaks at 654.6 and 643.3 eV, which are ascribed to the binding energies of (MnO_4) [47]. The composition as derived from XPS for elements of Mn-Zn_2SiO_4-48 is listed in Table 2. As can be seen, the atomic ratio of Mn^{2+}/Zn^{2+} is about 0.086, which is consistent with 0.08 of the original ratio in the experiment. The result suggests that the purity of Mn-Zn_2SiO_4-48 is high.

Table 2. Percentage composition of elements as calculated from XPS Results (Mn-Zn_2SiO_4-48).

Element	Peak BE	Height CPS	Area (P) CPS.eV	Atomic %
C 1s	284.80	14,204.3	36,722.61	17.64 (±1.00)
Mn 2p	654.60	2960.43	29,177.89	1.46 (±0.10)
O 1s	531.54	89,455.65	249,147.24	49.5 (±2.5)
Si 2p	102.52	11,412.33	31,207.52	14.93 (±1.00)
Zn 2p	1021.94	128,160.39	541,679.32	16.82 (±1.00)

3.3. Morphology and Microstructure

The typical SEM images of as-prepared samples are shown in Figure 4. It can be seen that the Mn-Zn_2SiO_4-12 sample is composed of agglomerated nanoparticles, with about 40 nm in Figure 4a. When the hydrothermal time is 24 h, the shuttle-like Mn-Zn_2SiO_4-24 with different lengths of rods can be found in Figure 4b. Obviously, due to the fusion between these nanoparticles, the rods were formed gradually. Further increasing the reaction time to 48 h, the rods were significantly lengthened, and the sample in Figure 4c consists of a large number of bundles. The average diameters and the lengths of nanorods were around 20 nm and 0.8–1.5 μm, respectively. When the sample was treated for 72 h, as observed in Figure 4d, owing to Ostwald ripening, the bundle of rods began to fuse together, and the diameter of the single rod increased to approximately 100 nm.

In order to further investigate the detailed character of the samples, TEM images of the different samples are shown in Figure 5. It can be observed from Figure 5a that Mn-Zn_2SiO_4-12 is composed of agglomerated nanoparticles. Further continuing the hydrothermal reaction time to 24 h, the enlarged view in Figure 5b shows that the nanorods come into being. Figure 5c shows that the length and diameter of the rods tend to grow when the reaction time is 48 h. As the reaction is treated for 72 h, a bundle of rods fuse together, and the diameter of the single rod is approximately 100 to 250 nm, as observed in

Figure 5d. Based on the Ostwald ripening mechanism, the diameter and length of the rods gradually increased with prolonging the hydrothermal time [48,49].

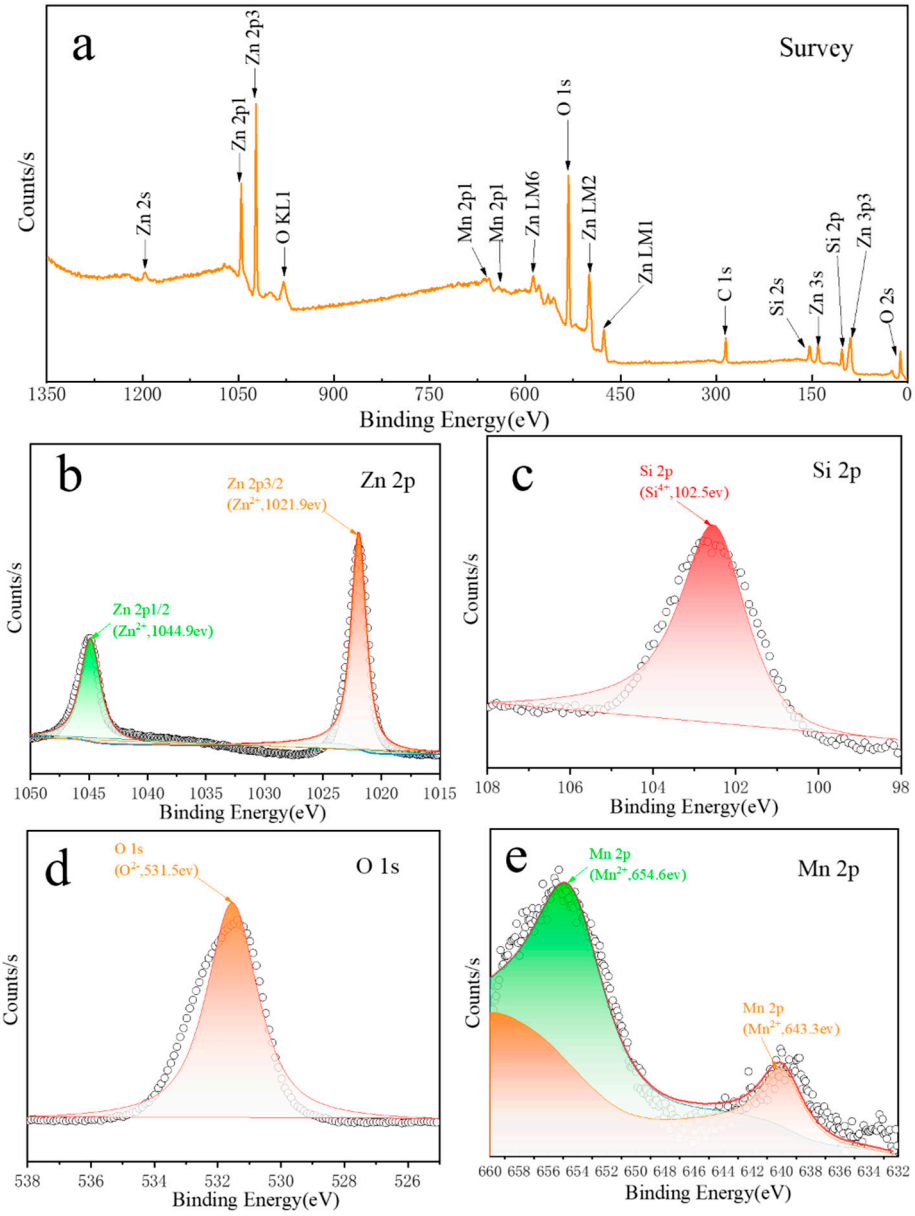

Figure 3. XPS spectra of Mn-Zn_2SiO_4-*48*: (**a**) survey, (**b**) Zn 2p, (**c**) Si 2p, (**d**) O 1s and (**e**) Mn 2p. (The black circle represents the actual data of the sample, and the other colors are the data after fitting).

Figure 6 shows the further enlarged HRTEM image of the nanorods in white squares range of Figure 5c. It is discovered that the nanorod is composed of many nanoparticles. Interestingly, these nanoparticles attach along the same direction, which shows mesocrystal characteristics. The Mn-Zn_2SiO_4-48 sample, being composed of individual nanoparticles, aggregated together to form a larger, fused mesoscopic crystal structure that behaved like a single crystal [50]. The lattice fringe observed in white circle range in Figure 6 is 0.659 nm, which agrees well with the lattice distance between the (110) lattice planes. Obviously, the nanorods have dominant growth along [001] direction, with a large number of structural defects from oriented attachment.

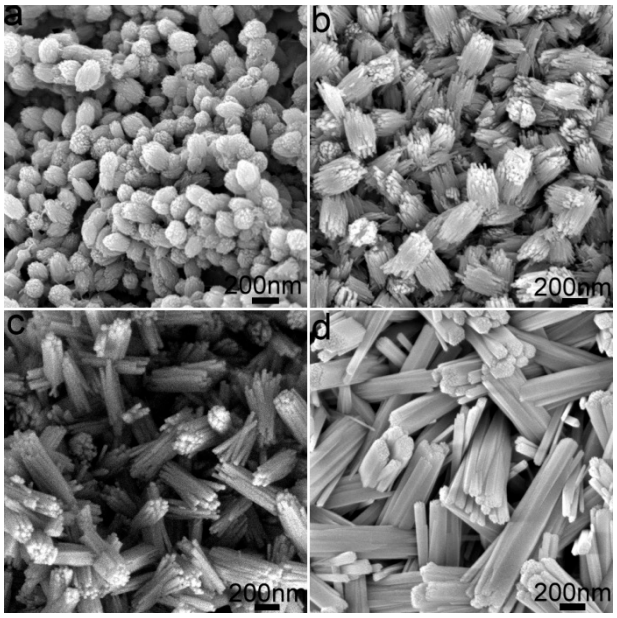

Figure 4. SEM images for Mn-Zn_2SiO_4-12 (**a**), Mn-Zn_2SiO_4-24 (**b**), Mn-Zn_2SiO_4-48 (**c**), and Mn-Zn_2SiO_4-72 (**d**).

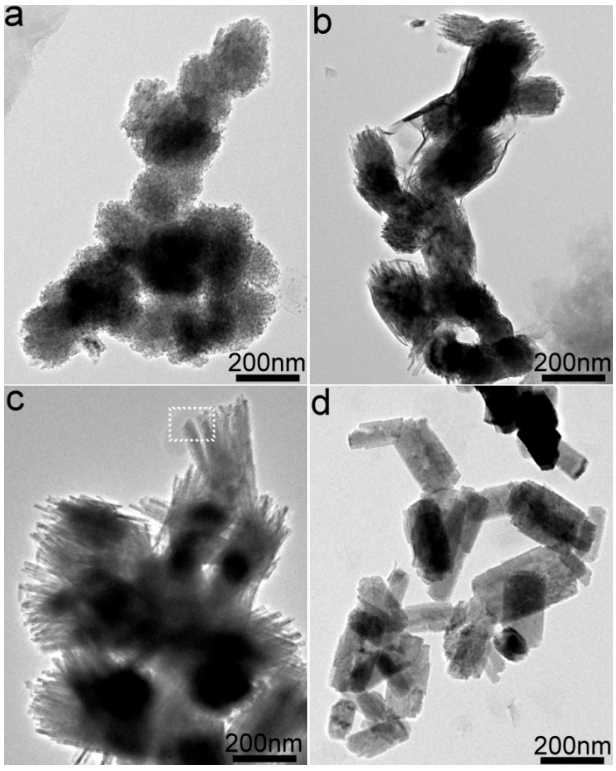

Figure 5. TEM images for Mn-Zn_2SiO_4-12 (**a**), Mn-Zn_2SiO_4-24 (**b**), Mn-Zn_2SiO_4-48 (**c**), and Mn-Zn_2SiO_4-72 (**d**).

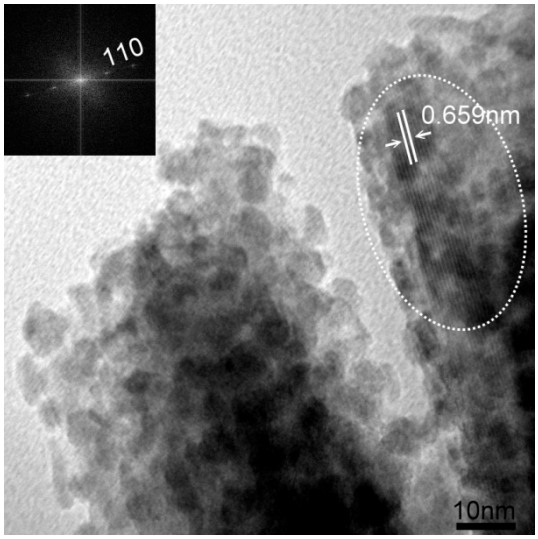

Figure 6. HRTEM for Mn-Zn_2SiO_4-48, the inset is FFT.

Based on the above analysis, the tentative growth process of the sheaf-like Mn-doped Zn_2SiO_4 is illustrated in Figure 7. In the beginning of the hydrothermal reaction, $Mn(OOCHC)_2$, $Zn(NO_3)_2 \cdot 6H_2O$ and $Na_2SiO_3 \cdot 9H_2O$ tend to form $Zn_{4-x}Mn_xSi_2O_7(OH)_2 \cdot H_2O$ bulk materials. As the reaction progressed, the bulk $Zn_{4-x}Mn_xSi_2O_7(OH)_2 \cdot H_2O$ gradually turned into $Zn_{4-x}Mn_xSiO_4$ nanoparticles as a result of H_2O molecules de-intercalating from the interlayer spaces of $Zn_{4-x}Mn_xSi_2O_7(OH)_2 \cdot H_2O$, along with a phase transformation from $Zn_{4-x}Mn_xSi_2O_7(OH)_2 \cdot H_2O$ to $Zn_{4-x}Mn_xSiO_4$ [41]. As the hydrothermal time prolonged, the $Zn_{4-x}Mn_xSiO_4$ nanoparticles vanished, and longer nanorods formed, owing to the "Ostwald ripening mechanism".

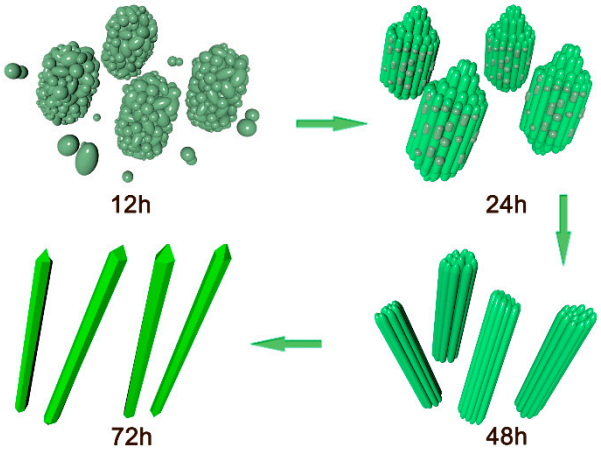

Figure 7. Schematic illustration of the hydrothermal process for the synthesis of sheaf-like Mn-doped Zn_2SiO_4.

3.4. Luminescence Properties

Based on the characteristics of the sample itself and the references [40,42,44], we finally chose 250 nm wavelength as the excitation light wavelength for the luminescence performance of the sample. As shown in Figure 8, the PL spectra of Mn-doped Zn_2SiO_4 phosphor were measured under the excitation of 250 nm at room temperature. The maximum emission peak is located at 522 nm due to the $4T^1$-$6A^1$ transition within d-orbital electrons, which is associated with the presence of Mn^{2+} in the Zn_2SiO_4 lattice [51,52]. It can also be observed that Mn-doped Zn_2SiO_4-48, namely sheaf-like Mn-doped Zn_2SiO_4, exhibits the highest peak strength due to the beam morphology. The reason is the result of the syner-

gistic effect of multiple factors. First of all, in contrast to rare-earth ion luminescence, for transition metal ions, the change in position symmetry does not have such a crucial effect on luminescence properties. The emission properties of manganese ions are determined by the crystal field of the host. The Gauss–Cauchy equation and HRTEM results show that Mn^{2+} replaces Zn^{2+} to form a luminescence center, occupying a low symmetry position and being in a distorted cationic environment. Mn^{2+} ion doping results in a large lattice distortion and structural defects in the Zn_2SiO_4 matrix, which is conducive to improving PL emission intensity [27,53,54]. Moreover, Mn-doped Zn_2SiO_4-48 samples have a unique mesomorphic structure, which is a bundle of small particles assembled into a higher specific surface area, so the role of surface defects is also greater. These defects (most commonly -oxygen vacancies) can act as electron traps that lead to the oxidation of Mn^{2+} ions to Mn^{3+} or Mn^{4+}. However, as the small particles assemble into larger, fused bundles of mesoscopic crystal structures, the relative number of oxygen vacancies decreases, and the possibility of manganese oxidation decreases. Due to the large surface-volume ratio, dense morphological characteristics, and nano-size effect, the bundle shape with long nanorods has a certain positive influence on the improvement of PL performance [55,56]. Furthermore, XPS tests show that the valence state of manganese is more in the +2 state, reflecting one of the reasons for the strong PL. In brief, the maximum brightness of Zn_2SiO_4-48 doped with bunched Mn is due to the unique bunched morphology, structural defects, large lattice distortion, and mesomorphic structure produced under the change in reaction conditions, and the synergistic effect of Mn^{2+} ions with stable valence of manganese ions is shown by XPS.

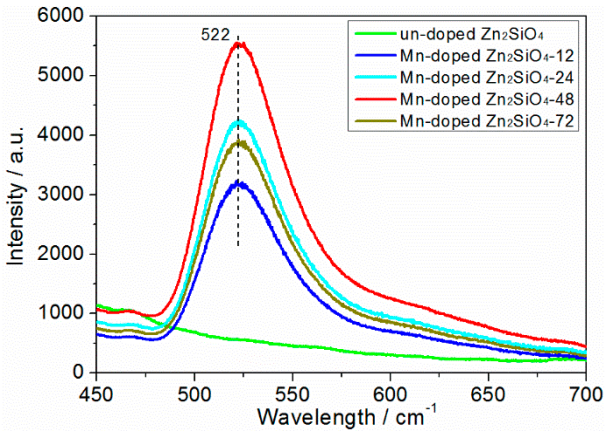

Figure 8. PL spectra of Mn $-Zn_2SiO_4$ obtained by different time under the excitation of 250 nm.

4. Conclusions

In summary, by controlling the atomic ratio of Mn^{2+}/Zn^{2+} to be around 0.08, we have successfully obtained sheaf-like Mn-doped Zn_2SiO_4 with excellent PL properties under hydrothermal times of 48 h. It is interesting to find that the reacting time has a great influence on the morphology and crystallinity of as-prepared samples. The sheaf-like Mn-doped Zn_2SiO_4 shows a high PL intensity mainly owing to the synergistic effect of unique sheaf-like morphology, structural defects, large lattice distortion, and mesomorphic structure, and the synergistic effect of Mn^{2+} ions with stable valence of manganese ions shown by XPS. The above result offered a new idea to modify the PL property of phosphor materials.

Author Contributions: Conceptualization, X.L.; methodology, X.L., X.Z. and H.Z.; software, Y.Y. and L.W.; validation, Y.Y. and R.L.; formal analysis, X.L. and Y.Y.; investigation, X.L. and S.C.; resources, X.Z. and H.Z.; data curation, X.L.; writing—original draft preparation, X.L.; writing—review and editing, X.L., Y.Y. and H.Z.; visualization, R.C. and R.L.; supervision, X.Z. and H.Z.; project administration, X.Z.; funding acquisition, X.Z. and H.Z. All authors have read and agreed to the published version of the manuscript.

Funding: We would like to express our gratitude for the financial support from National Natural Science Foundation of China (No. 52062020), Science and Technology Research Project of Jiangxi Provincial Education Department (Nos. GJJ211317, GJJ2201015 and GJJ2201052) and Jingdezhen City Science and Technology Project (Nos. 20224SF005-11 and 2022GY008-09), Jiangxi Provincial key research and development program (No. 20202BBE53011).

Data Availability Statement: The data presented in this study are available on request from the corresponding author. The data are not publicly available due to privacy.

Conflicts of Interest: The authors declare no conflict of interest.

References

1. Kong, D.; Zhang, K.; Tian, J.; Yin, L.; Sheng, X. Biocompatible and biodegradable light-emitting materials and devices. *Adv. Mater. Technol.* **2022**, *7*, 2100006. [CrossRef]
2. Wang, Q.; Liao, M.; Lin, Q.; Xiong, M.; Mu, Z.; Wu, F. A review on fluorescence intensity ratio thermometer based on rare-earth and transition metal ions doped inorganic luminescent materials. *J. Alloy Compd.* **2021**, *850*, 156744. [CrossRef]
3. Wang, D.; Chen, L.; Jiang, L.; Yu, Y.; Lu, Y.; Li, H.; Li, Y.; Meng, Z.; Su, Q.; Zhang, Y.; et al. A high temperature macroscopically flexible inorganic $CaYAl_3O_7$:Eu^{3+} nanofiber luminescent membrane. *J. Mater. Chem. C* **2022**, *10*, 7594. [CrossRef]
4. Medintz, I.L.; Uyeda, H.T.; Goldman, E.R.; Mattoussi, H. Quantum dot bioconjugates for imaging, labelling and sensing. *Nat. Mater.* **2005**, *4*, 435–446. [CrossRef] [PubMed]
5. Huang, F.; Chen, D. Synthesis of Mn^{2+}: Zn_2SiO_4-Eu^{3+}: Gd_2O_3 nanocomposites for highly sensitive optical thermometry through the synergistic luminescence from lanthanide-transition metal ions. *J. Mater. Chem. C* **2017**, *5*, 5176–5182. [CrossRef]
6. Shen, C.; Yang, Y.; Jin, S.; Ming, J. Luminous characteristics and thermal stability of $BaMgAl_{10}O_{17}$: Eu^{2+} phosphor for white light-emitting diodes. *Phys. B Condens. Matter.* **2010**, *405*, 1045–1049. [CrossRef]
7. Polisadova, E.; Valiev, D.; Vaganov, V.; Oleshko, V.; Han, T.; Zhang, C.; Burachenko, A.; Popov, A.I. Time-resolved cathodoluminescence spectroscopy of YAG and YAG: Ce^{3+} phosphors. *Opt. Mater.* **2019**, *96*, 109289. [CrossRef]
8. Karipbayev, Z.T.; Lisitsyn, V.M.; Mussakhanov, D.A.; Alpyssova, G.K.; Popov, A.I.; Polisadova, E.F.; Elsts, E.; Akilbekov, A.T.; Kukenova, A.B.; Kemere, M.; et al. Time-resolved luminescence of YAG: Ce and YAGG: Ce ceramics prepared by electron beam assisted synthesis. *Nucl. Instrum. Methods Phys. Res. Sect. B Beam Interact. Mater. At.* **2020**, *479*, 222–228. [CrossRef]
9. Xie, B.; Lei, L.; Liu, E.; Bai, G.; Ye, R.; Xu, S. Blue-LED-excited Ce^{3+}-doped alkaline-earth sulfide luminescent nanocrystals for selective and sensitive Fe^{3+} ions sensing. *J. Lumin.* **2021**, *230*, 117740. [CrossRef]
10. Zhao, D.; Zhang, S.-R.; Fan, Y.-P.; Liu, B.-Z.; Li, Y.-N.; Shi, L.-Y.; Dai, S.-J. Two-Site Occupancy Induced a Broad-Band Emission in Phosphor K_2YZr $(PO_4)_3$: Eu^{2+} for White-Light-Emitting Diode Applications. *ACS Sustain. Chem. Eng.* **2020**, *8*, 18992–19002. [CrossRef]
11. Changshuai, G.O.G.; Xuyan, X.U.; Xiaowen, F.E.G.; Jiantong, W.A.G.; Bowen, W.A.G.; Xuejiao, W.A.G. UP-conversion photo luminescence of $(La_{0.88}Yb_{0.10}Ho_{0.02})_2W_2O_9$ phosphor and dual-mode thermometry. *J. Funct. Mater.* **2023**, *3*, 03179–03186.
12. Lacorre, P.; Goutenoire, F.; Bohnke, O.; Retoux, R.; Laligant, Y. Designing fast oxide-ion conductors based on $La_2Mo_2O_9$. *Nature* **2000**, *404*, 856–858. [CrossRef] [PubMed]
13. Kaur, H.; Jayasimhadri, M. Color tunable photo luminescence properties in Eu^{3+} doped calcium bismuth vanadate phosphors for luminescent devices. *Ceram. Int.* **2019**, *45*, 15385–15393. [CrossRef]
14. Chernov, S.A.; Trinkler, L.; Popov, A.I. Photo-and thermo-stimulated luminescence of CsI-Tl crystal after UV light irradiation at 80 K. *Radiat. Eff. Defects Solids* **1998**, *143*, 345–355. [CrossRef]
15. Sun, J.; Zhang, X.; Du, H. Combustion synthesis and luminescence properties of blue $NaBaPO_4$:Eu^{3+} phosphor. *J. Rare Earths* **2012**, *30*, 118–122. [CrossRef]
16. Kozhevnikova, N.M.; Batueva, S.Y. Synthesis of a $LiZnSc(MoO_4)_3$:Eu^{3+}-based red phosphor. *Inorg. Mater.* **2019**, *55*, 59–63. [CrossRef]
17. Aleksandrova, L.; Iordanovaa, R.; Dimitrievbetal, Y.; Georgiev, N.; Komatsu, T. Eu^{3+} doped $1La_2O_3$:$2WO_3$:$1B_2O_3$ glass and glass–ceramic. *Opt. Mater.* **2014**, *36*, 1366–1372. [CrossRef]
18. Yu, M.; Lin, J.; Fang, J. Silica spheres coated with YVO_4: Eu^{3+} layers via sol-gel process: A simple method to obtain spherical core-shell phosphors. *Chem. Mater.* **2005**, *17*, 1783–1791. [CrossRef]
19. Quan, L.N.; Rand, B.P.; Friend, R.H.; Mhaisalkar, S.G.; Lee, T.W.; Sargent, E.H. Perovskites for next-generation optical sources. *Chem. Rev.* **2019**, *119*, 7444–7477. [CrossRef]
20. Liu, X.K.; Xu, W.; Bai, S.; Jin, Y.; Wang, J.; Friend, R.H.; Gao, F. Metal Halide Perovskites for Light-Emitting Diodes. *Nat. Mater.* **2021**, *20*, 10–21. [CrossRef]
21. Yao, J.S.; Wang, J.J.; Yang, J.N.; Yao, H.B. Modulation of Metal Halide Structural Units for Light Emission. *Acc. Chem. Res.* **2021**, *54*, 441–451. [CrossRef] [PubMed]
22. He, X.; Zhang, H.; Xie, F.; Tao, C.; Xu, H.; Zhong, S. Enhanced afterglow performance of Zn_2SiO_4:Mn^{2+} by Pr^{3+} doping and mechanism. *Ceram. Int.* **2022**, *48*, 19358–19366. [CrossRef]
23. Uegaito, K.; Hosokawa, S.; Inoue, M. Effect of heat treatments on the luminescence properties of Zn_2SiO_4: Mn^{2+} phosphors prepared by glycothermal methods. *J. Lumin.* **2012**, *132*, 64–70. [CrossRef]

24. Barthou, C.; Benoit, J.; Benalloul, P.; Morell, A. Mn^{2+} concentration effect on the optical properties of Zn_2SiO_4: Mn phosphors. *J. Electrochem. Soc.* **1994**, *141*, 524. [CrossRef]
25. Yoshizawa, K.; Kato, H.; Kakihana, M. Synthesis of Zn_2SiO_4:Mn^{2+} by homogeneous precipitation using propylene glycol-modified silane. *J. Mater. Chem.* **2012**, *22*, 17272–17277. [CrossRef]
26. Liu, H.; Moronta, D.; Li, L.; Yue, S.; Wong, S.S. Synthesis, properties, and formation mechanism of Mn-doped Zn_2SiO_4 nanowires and associated heterostructures. *Phys. Chem. Chem. Phys.* **2018**, *20*, 10086–10099. [CrossRef] [PubMed]
27. Bharti, D.K.; Verma, R.; Rani, S.; Agarwal, D.; Mehra, S.; Gangwar, A.K.; Gupta, B.K.; Singh, N.; Srivastava, A.K. Synthesis and characterization of highly crystalline Bi-functional Mn-doped Zn_2SiO_4 nanostructures by low-cost sol-gel process. *Nanomaterials* **2023**, *13*, 538. [CrossRef]
28. Kim, J.S.; Kwon, A.K.; Park, Y.H.; Choi, J.C.; Park, H.L.; Kim, G.C. Luminescent and thermal properties of full-color emitting $X_3MgSi_2O_8$:Eu^{2+}, Mn^{2+} (X=Ba, Sr, Ca) phosphors for white LED. *J. Lumin.* **2007**, *122–123*, 583–586. [CrossRef]
29. Zhao, M.; Xia, Z.; Huang, X.; Ning, L.; Gautier, R.; Molokeev, M.S.; Zhou, Y.; Chuang, Y.C.; Zhang, Q.; Liu, Q.; et al. Li substituent tuning of LED phosphors with enhanced efficiency, tunable photoluminescence, and improved thermal stability. *Sci. Adv.* **2019**, *5*, 0363. [CrossRef]
30. Song, E.H.; Zhou, Y.Y.; Wei, Y.; Han, X.X.; Tao, Z.R.; Qiu, R.L.; Xia, Z.G.; Zhang, Q.Y. A thermally stable narrow-band green-emitting phosphor $MgAl_2O_4$:Mn^{2+} for wide color gamut backlight display application. *J. Mater. Chem. C* **2019**, *7*, 8192–8198. [CrossRef]
31. Hu, T.; Lin, H.; Xu, J.; Wang, B.; Wang, J.; Wang, Y. Color-tunable persistent luminescence in oxyfluoride glass and glass ceramic containing Mn^{2+}: α-Zn_2SiO_4 nanocrystals. *J. Mater. Chem. C* **2017**, *5*, 1479–1487. [CrossRef]
32. El Mir, L. Sol-gel synthesis and luminescence of undoped and Mn-doped zinc orthosilicate phosphor nanocomposites. *J. Lumin.* **2014**, *148*, 82–88.
33. Lin, L.; Feiyan, X.; Dekang, X.; Chaochao, T.; Hualan, X.; Zhong, S. Zn_2SiO_4: Mn^{2+}, Yb^{3+} long afterglow materials prepared employing Zn-based coordination polymer as precursor: Properties, Mechanism and Application. *J. Lumin.* **2023**, *255*, 119601.
34. Omri, K.; Lemine, O.M.; El Mir, L. Mn doped zinc silicate nanophosphor with bifunctionality of green-yellow emission and magnetic properties. *Ceram. Int.* **2017**, *43*, 6585–6591. [CrossRef]
35. Lu, Q.; Wang, P.; Li, J. Structure and luminescence properties of Mn-doped Zn_2SiO_4 prepared with extracted mesoporous silica. *Mater. Res. Bull.* **2011**, *46*, 791–795. [CrossRef]
36. El Ghoul, J.; El Mir, L. Synthesis by sol-gel process, structural and luminescence of V and Mn doped a-Zn_2SiO_4. *J Mater. Sci. Mater. Electron.* **2015**, *26*, 3550–3557. [CrossRef]
37. Su, K.; Tilley, T.D.; Sailor, M.J. Molecular and polymer precursor routes to manganese-doped zinc orthosilicate phosphors. *J. Am. Chem. Soc.* **1996**, *118*, 3459–3468. [CrossRef]
38. Yoo, J.B.; Yang, H.J.; Hur, N.H. Controlled synthesis of luminescent Mn-doped Zn_2SiO_4 microspheres by thermal hydrolysis of urea. *J. Lumin.* **2022**, *243*, 118608. [CrossRef]
39. Xu, G.Q.; Xu, H.T.; Zheng, Z.X.; Wu, Y.C. Preparation and characterization of Zn_2SiO_4: Mn phosphors with hydrothermal methods. *J. Lumin.* **2010**, *130*, 1717–1720. [CrossRef]
40. Cho, J.S.; Lee, S.M.; Jung, K.Y.; Kang, Y.C. Large-scale production of fine-sized Zn_2SiO_4: Mn phosphor microspheres with a dense structure and good photoluminescence properties by a spray-drying process. *RSC Adv.* **2014**, *4*, 43606–43611. [CrossRef]
41. Zhang, S.; Ren, L.; Peng, S. Zn_2SiO_4 urchin-like microspheres: Controlled synthesis and application in lithium-ion batteries. *CrystEngComm* **2014**, *16*, 6195–6202. [CrossRef]
42. Xiong, L.; Shi, J.; Gu, J.; Shen, W.; Dong, X.; Chen, H.; Zhang, L.; Gao, J.; Ruan, M. Directed growth of well-aligned zinc silicate nanowires along the channels of surfactant-assembled mesoporous silica. *Small* **2005**, *1*, 1044–1047. [CrossRef] [PubMed]
43. Wan, J.; Chen, X.; Wang, Z.; Mu, L.; Qian, Y. One-dimensional rice-like Mn-doped Zn_2SiO_4: Preparation, characterization, luminescent properties and its stability. *J. Cryst. Growth* **2005**, *280*, 239–243. [CrossRef]
44. Wang, H.; Ma, Y.; Yi, G.; Chen, D. Synthesis of Mn-doped Zn_2SiO_4 rodlike nanoparticles through hydrothermal method. *Mater. Chem. Phys.* **2003**, *82*, 414–418. [CrossRef]
45. Ahmadi, T.S.; Haase, M.; Weller, H. Low-temperature synthesis of pure and Mn-doped willemite phosphor (Zn_2SiO_4: Mn) in aqueous medium. *Mater. Res. Bull.* **2000**, *35*, 1869–1879. [CrossRef]
46. Klug, H.P.; Alexander, E. *X-ray Diffraction Procedures: For Polycrystalline and Amorphous Materials*; Wiley-VCH: Weinheim, Germany, 1974; Volume 5, p. 992. ISBN 0-471-49369-4.
47. Hafeez, M.; Ali, A.; Manzoora, S.; Bhatti, A.S. Anomalous optical and magnetic behavior of multi-phase Mn doped Zn_2SiO_4 nanowires: A new class of dilute magnetic semiconductors. *Nanoscale* **2014**, *6*, 14845–14855. [CrossRef]
48. Peng, Z.A.; Peng, X.G. Mechanisms of the shape evolution of CdSe nanocrystals. *J. Am. Chem. Soc.* **2001**, *123*, 1389–1395. [CrossRef]
49. Ma, H.; Zhang, S.Y.; Ji, W.Q.; Tao, Z.L.; Chen, J. α-CuV_2O_6 nanowires: Hydrothermal synthesis and primary lithium battery application. *J. Am. Chem. Soc.* **2008**, *130*, 5361–5367. [CrossRef]
50. Zhu, G.; Sushko, M.L.; Loring, J.S.; Legg, B.A.; Song, M.; Soltis, J.A.; Huang, X.; Rosso, K.M.; De Yoreo, J.J. Self-similar mesocrystals form via interface-driven nucleation and assembly. *Nature* **2021**, *590*, 416–422. [CrossRef]
51. Lee, D.H.; Wang, W.; Gutu, T.; Jeffryes, C.; Rorrer, G.L.; Jiao, J.; Chang, C.H. Biogenic silica based Zn_2SiO_4: Mn^{2+} and Y_2SiO_5: Eu^{3+} phosphor layers patterned by inkjet printing process. *J. Mater. Chem.* **2008**, *18*, 3633–3635. [CrossRef]

52. Bhalla, R.; White, E.W. Cathodoluminescence Characteristics of Mn^{2+}-Activated Willemite (Zn_2SiO_4) Single Crystals. *J. Electrochem. Soc.* **1972**, *119*, 740–743. [CrossRef]
53. Wu, B.; Li, J.; Li, Q. Preparation and photoluminescence behavior of Mn-doped nano-ZnO. *Optik* **2019**, *188*, 205–211. [CrossRef]
54. Bulyk, L.I.; Vasylechko, L.; Mykhaylyk, V.; Tang, C.; Zhydachevskyy, Y.; Hizhnyi, Y.A.; Nedilko, S.G.; Klyui, N.I.; Suchocki, A. Mn^{2+} luminescence of Gd (Zn, Mg) B_5O_{10} pentaborate under high pressure. *Dalton Trans.* **2020**, *49*, 14268–14279. [CrossRef]
55. Gavrilović, T.; Periša, J.; Papan, J.; Vuković, K.; Smits, K.; Jovanović, D.J.; Dramićanin, M.D. Particle size effects on the structure and emission of Eu^{3+}: $LaPO_4$ and $EuPO_4$ phosphors. *J. Lumin.* **2018**, *195*, 420–429. [CrossRef]
56. Hou, Z.Y.; Li, G.G.; Lian, H.Z.; Liu, J. One-dimensional luminescent materials derived from the electrospinning process: Preparation, characteristics and application. *J. Mater. Chem.* **2012**, *22*, 5254–5276. [CrossRef]